International Journal of Engineering Research & Technology (IJERT)
ISSN: 2278-0181
Vol. 14, Issue 08, IESAME - 2026

# Development of a Multi-Degree-of-Freedom Morphing Wing UAV using Compliant PLA Ribs and Active Servo Actuation

**Srinuvasu. N, Purnima Birangi , Archana M, Bharath Kumar S , Alagu Sundram.A, Balaraja NC , Byre Gowda KC**

**Srinuvas.n@gmail.com, Srinuvasu.me@drait.edu.in**

Orchid id 0009-0002-5457-6411

**Srinuvasu.N** - Mechanical Department, Assistant professor Dr Ambedkar institute of technology Bangalore 56
**Purnima Birangi** - Civil engg asst professor Dr Ambedkar institute of technology Bangalore 56
**Archana M** - Aeronautical engg Department, Dr Ambedkar institute of technology Bangalore 56
**Bharath Kumar** - Aeronautical engg Department, Dr Ambedkar institute of technology Bangalore 56
**Alagu sundaram A** - Aeronautical engg Department, Dr Ambedkar institute of technology Bangalore 56 **Balaraja NC** - Aeronautical engg Department, Dr Ambedkar institute of technology Bangalore 56
**Byre gowda KC** - Mechanical Department, Assistant professor Dr Ambedkar institute of technology Bangalore 56
**Byre Gowda** - Mechanical Department, Dr Ambedkar institute of technology Bangalore 56

**Abstract** - ***This paper presents the design, structural modeling, and aerodynamic characterization of a multi-degree-of-freedom (DOF) morphing wing concept utilizing an asymmetrical NACA 4418 baseline aerofoil. The wing features a continuous, variable-camber trailing edge driven by localized digital servo motors integrated with compliant sliding runners. By replacing traditional discrete, hinged control surfaces with a seamless, flexible polylactic acid (PLA) composite truss structure, the wing maintains surface continuity during geometric deflection. Nonlinear finite element (FE) simulations demonstrate that the compliant internal skeleton exhibits robust load-carrying capabilities under structural loads up to 250\text{ N}. Aerodynamic evaluations performed via XFOIL quantify lift-to-drag (L/D) ratio enhancements across multiple morphing strategies at low Reynolds numbers (Re = 0.5 \times 10^5 to 1.5 \times 10^5), representative of small unmanned aerial vehicles (UAVs). The work demonstrates that independent control of localized camber distributions enables independent pitching-moment control and broadens the operational flight envelope of tactical micro-UAVs. Finally, physical prototyping and benchtop static load testing validate the structural resilience, deflection accuracy, and manufacturing feasibility of the proposed compliant mechanism.***

*Index Terms*—**Adaptive aerofoil, compliant truss, morphing wing, multi-degree-of-freedom, servo motors, low Reynolds number aerodynamics.**

## I. INTRODUCTION

To optimize the aerodynamic and operational efficiency of unmanned aerial vehicles (UAVs) across diverse mission profiles—such as high-speed transit, low-speed loitering, and high-g maneuvering—the lift and drag forces acting on the wing surfaces must be dynamically adjusted. Traditionally, these adjustments are achieved using hinged discrete control surfaces, such as flaps, ailerons, and spoilers. However, the sharp surface discontinuities and localized high curvature introduced by hinged deflections provoke premature boundary-layer separation. This flow separation results in substantial parasitic drag penalties, aerodynamic

International Journal of Engineering Research & Technology (IJERT)
ISSN: 2278-0181
Vol. 14, Issue 08, IESAME - 2026

noise, and premature stall, imposing strict constraints on the vehicle's flight envelope and fuel efficiency. Wing morphing, which enables continuous changes in aerofoil geometry while maintaining a smooth and seamless aerodynamic surface, has the potential to overcome these limitations. Wind tunnel evaluations indicate that substituting conventional hinged flaps with a continuously deforming morphing trailing edge can enhance the lift-to-drag (L/D) ratio of a two-dimensional aerofoil by 20\% to 25\%. Despite these benefits, historical research has predominantly focused on single-degree-of-freedom morphing systems, such as simple droop-nose or trailing-edge deflections. This focus has left the potential benefits of multi-degree-of-freedom camber line adaptations, which offer multiple localized morphing strategies, largely unaddressed.

The structural implementation of a variable-camber morphing wing is fundamentally constrained by conflicting requirements. The internal skeleton must exhibit high compliance along the morphing axis to minimize actuation power, yet it must maintain high stiffness in the out-of-plane direction to withstand aerodynamic pressure distributions without excessive structural deflection. To satisfy these requirements, various structural concepts have been explored, including topology-optimized compliant mechanisms , adaptive "belt-rib" structures , and smart materials such as shape memory alloys (SMAs) and piezoelectric micro-fiber composites (MFCs). However, SMAs suffer from low thermodynamic cycle frequencies, thermal hysteresis, and high power draw during sustained deflection. Piezoelectric ceramics deliver rapid response rates but are limited by extremely small strain outputs (typically \sim0.1\%), requiring complex, heavy displacement amplification mechanisms.

To overcome these limitations, this paper proposes an active trailing-edge morphing wing concept based on a compliant PLA composite truss structure. While previous high-end concepts propose linear ultrasonic motors (LUSMs) to drive compliant runners , this study evaluates the implementation of high-performance, cost-effective rotary servo motors with closed-loop positional feedback. This actuation framework enables precise, independent control of multiple chordwise structural joints, allowing for real-time camber modifications with multiple degrees of freedom.

## II. PROPOSED MORPHING WING ARCHITECTURE

### A. Comparative Evaluation of Actuation Systems

The integration of localized actuators within a thin, aerodynamic wing profile requires a careful trade-off between output torque, power density, structural weight, and holding capabilities. In high-altitude or tactical military UAVs, specialized linear ultrasonic motors (such as the SPL-801) provide high holding torque without power draw by utilizing piezoelectric friction-drive interfaces. However, for small, cost-constrained tactical or civilian micro-UAVs, off-the-shelf servo motors present a compelling alternative. High-torque digital servos, such as the DS3218 and HS-7954SH, incorporate integrated potentiometers and gear trains that deliver high torque density and precise positioning.

A comparison of off-the-shelf actuation systems is provided in Table I, contrasting digital servo motors with piezoelectric ultrasonic motors, brushless DC motors, and geared DC transmissions.

| Actuator Model | Actuator Type | Output Torque (\text{kg}\cdot\text{cm}) | Holding Torque (\text{kg}\cdot\text{cm}) | Rated Velocity (\text{rpm}) | Mass (\text{g}) | Power Density (\text{W/kg}) |
|---|---|---|---|---|---|---|
| **DS3218** | Digital Servo | 10.0 | 10.0 | 60 | 60 | 80 |

International Journal of Engineering Research & Technology (IJERT)
ISSN: 2278-0181
Vol. 14, Issue 08, IESAME - 2026

| | | | | | | |
|---|---|---|---|---|---|---|
| **HS-7954SH** | Coreless Servo | 24.0 | 24.0 | 40 | 68 | 120 |
| **SPL-801** | Piezoelectric USM | 10.0 | N/A | 210 | 249 | 95 |
| **Maxon Brushless** | DC Motor | 0.076 | N/A | 25,000 | 86 | 235 |
| **Geared DC** | DC with | 32.0 | N/A | 60 | 739 | 27 |
| Actuator Model | Actuator Type | Output Torque (\text{kg}\cdot t\text{cm}) | Holding Torque (\text{kg}\cdot t\text{cm}) | Rated Velocity (\text{rpm}) | Mass (\text{g}) | Power Density (\text{W/kg}) |
| **System** | Harmonic Gear | | | | | |

*Table I: Comparative assessment of actuation technologies for UAV wing morphing.* While brushless DC motors achieve superior bare power density, their high rotational speeds require extremely high gear-reduction ratios (such as harmonic or planetary gearboxes), which increases system weight, volume, and mechanical complexity. Conversely, high-torque digital servos supply a balanced operational envelope, offering high holding torque through active closed-loop positional control. This holding torque is critical to resist aerodynamic hinge moments and prevent control surface flutter under high dynamic pressure conditions.

## B. Kinematic Truss and Skeleton Design

The baseline wing geometry selected for this design is the asymmetric NACA 4418 aerofoil. This profile is chosen due to its relatively large thickness-to-chord ratio (18\%) and its nearly flat lower surface. These geometric properties simplify the placement of internal actuators and sliding compliant runners while maintaining the structural volume required for high-torque servo motors.

The internal structural layout of the active trailing-edge wing is illustrated schematically in Figure 1.

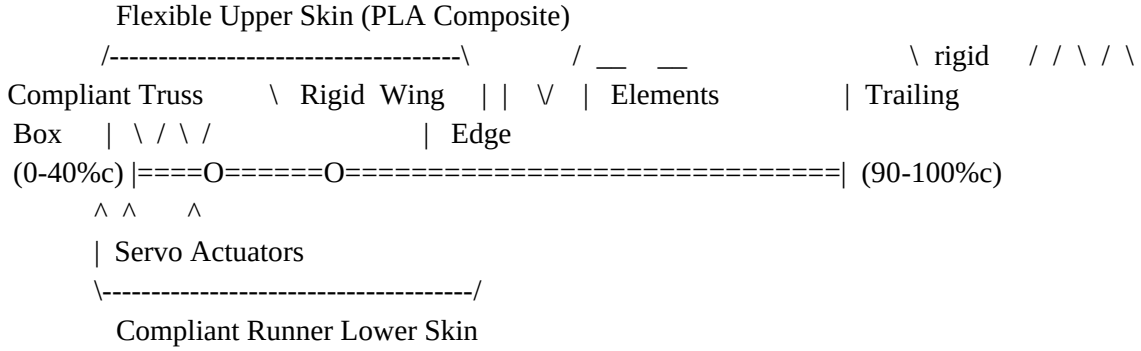

International Journal of Engineering Research & Technology (IJERT)
ISSN: 2278-0181
Vol. 14, Issue 08, IESAME - 2026

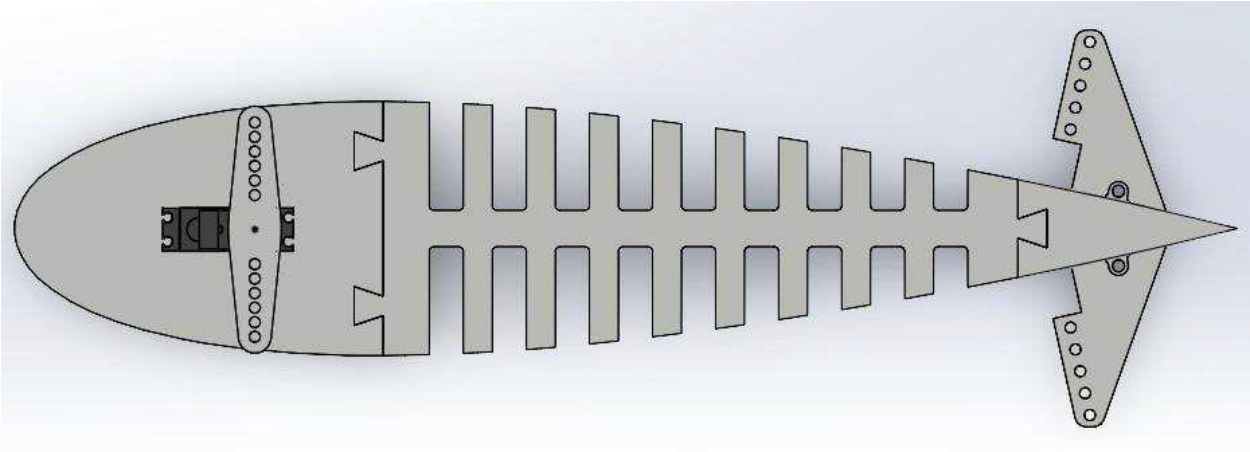

*Figure 1: Internal structural skeleton and kinematic layout of the variable-camber morphing wing.*

The wing is structurally partitioned into three primary zones along the chordwise direction :

1. **Rigid Wing Box (0% to 40% chord):** A stiff, non-deforming leading-edge assembly that resists primary torsional and bending flight loads.
2. **Morphing Section (40% to 90% chord):** A flexible section comprising a compliant, continuous upper skin, four independent compliant truss elements, and three localized servo motor assemblies.
3. **Rigid Trailing Edge (90% to 100% chord):** A thin, rigid termination section that ensures clean aerodynamic flow separation.

The four compliant truss elements are hinged directly to the flexible upper skin. To prevent lateral mechanical interference between neighboring components during large structural deflections, the trusses are shifted in the span-wise direction. A vertex angle of 60^\\circ is maintained between adjacent truss elements. This angle represents an optimal compromise between localized out-of-plane structural stiffness and the kinematic displacement range of the actuators. The servo actuators are positioned at the bottom apexes of the truss elements. One or more compliant runners (fabricated from high-strength composite or high-modulus PLA) are anchored to the rigid trailing edge and pass through the drive paths of the servo motors.

When the servos are activated, they drive the compliant runners relative to the truss apexes.

This sliding action forces the compliant skeleton to flex, modifying the camber of the aerofoil. Because the upper skin is highly flexible and the lower skin is formed by the compliant runners, the aerofoil surface maintains a smooth, continuous curvature during deformation, minimizing aerodynamic drag penalties.

## III. NUMERICAL STRUCTURAL ANALYSIS

### A. Finite Element Modeling of Morphing Kinematics

To evaluate the structural behavior and kinematic accuracy of the morphing mechanism, a nonlinear, large-deflection finite element (FE) simulation was performed. In the FE model, the hinges connecting the compliant truss elements to the flexible upper skin were assumed to have negligible rotational resistance, simulating pin-joint behavior. Actuator displacement was modeled through equivalent localized thermal contraction and expansion of the compliant runners. This boundary condition accurately captures the mechanical deformation of the wing skeleton while reducing computational times compared to modeling the contact friction of the motor-runner interface.

International Journal of Engineering Research & Technology (IJERT)
ISSN: 2278-0181
Vol. 14, Issue 08, IESAME - 2026

The structural mass of the deforming morphing section (excluding the rigid wing box) was determined to be 22\text{ g} for a reference span of 50\text{ mm}, which translates to an equivalent structural weight of 440\text{ g/m} of wing span. The non-linear FE kinematic simulation of a near-maximum downward trailing-edge deflection is shown in Figure 2.

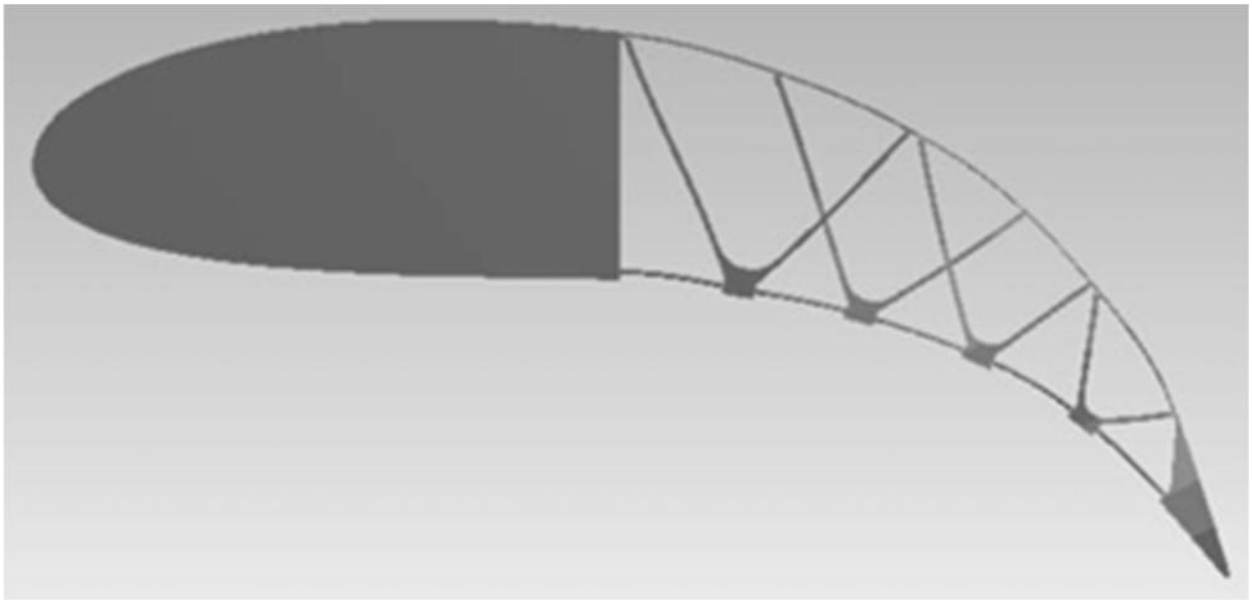

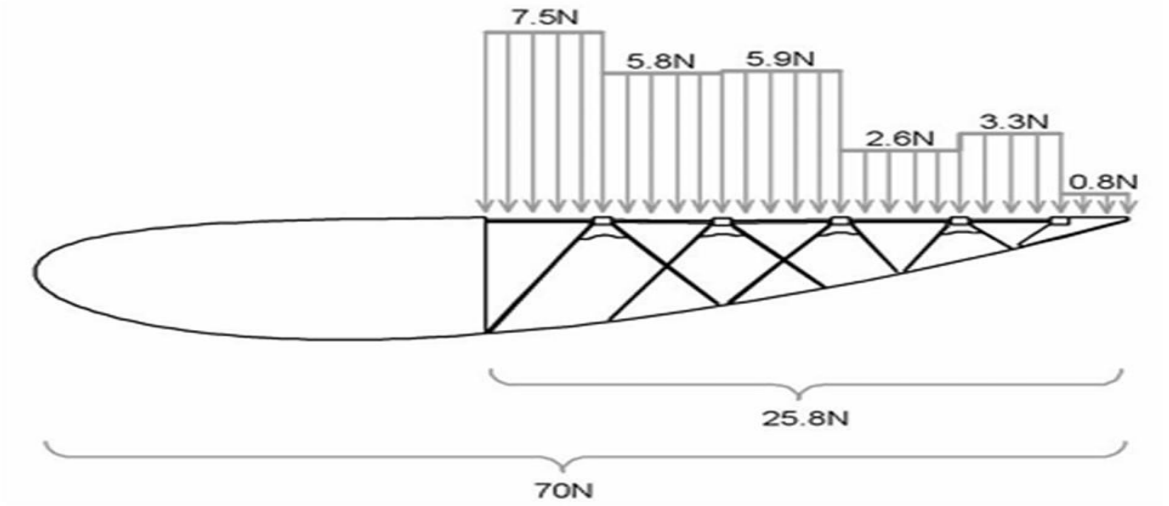



/ ___

International Journal of Engineering Research & Technology (IJERT)
ISSN: 2278-0181
Vol. 14, Issue 08, IESAME - 2026

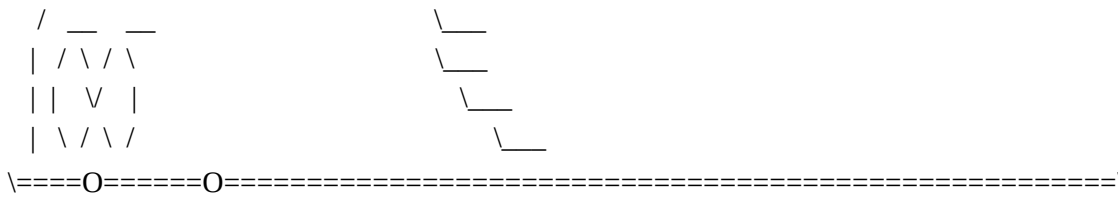

*Figure 2: Finite element deformation profile showing smooth upper skin curvature at high trailing-edge deflection.*

The FE analysis revealed minor localized surface waviness along both the upper skin and the sliding lower runners under extreme deflection states. Computational fluid dynamics studies indicate that a localized surface protuberance situated behind the mid-chord position has a negligible impact on overall lift and drag forces, provided the maximum height of the wave remains below 0.5\% of the total chord length (c). In the simulated model, the maximum waviness height was confined within this limit, verifying that the mechanical deformation would not degrade aerodynamic performance.

## B. Static Load Capacity and Deflection Evaluations

A critical challenge in morphing wing design is ensuring the structure can carry aerodynamic lift loads without collapsing or undergoing excessive parasitic deformation. To quantify the load-carrying capacity of the design, a nonlinear static structural simulation was conducted. An aerodynamic load distribution was calculated using XFOIL. The continuous lift pressure distribution acting on the flexible morphing section was simplified into six discrete force vectors applied to the lower surface of the structural model. The magnitude of these forces represents an integrated chordwise load distribution, with the bulk of the lift force concentrated near the forward portion of the morphing section. This loading profile is illustrated schematically in Figure 3.

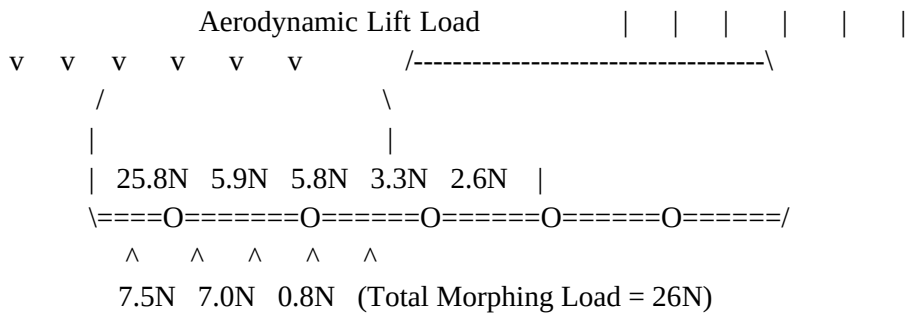


*Figure 3: Concentrated load distribution applied during static finite element testing.*

Using this loading method, three separate structural flight states were simulated, corresponding to total lift loads of 70\text{ N}, 130\text{ N}, and 250\text{ N} across the entire aerofoil surface. Due to the forward concentration of aerodynamic lift, the rear morphing section carried localized loads of 26\text{ N}, 48\text{ N}, and 93\text{ N}, respectively.

The resulting deflection metrics, deflection-to-chord ratios, and equivalent flight operating conditions are compiled in Table II.

| Total Applied Load (\text{N}) | Local Morphing Load (\text{N}) | Max Out-of-Plane Deflection (\text{mm}) | Deflection / Chord Ratio (\%) | Equivalent Flight Condition | Notes / Safety Factors |
|---|---|---|---|---|---|

International Journal of Engineering Research & Technology (IJERT)
ISSN: 2278-0181
Vol. 14, Issue 08, IESAME - 2026

| | | | | | |
|---|---|---|---|---|---|
| **70** | 26 | 0.36 (0.2 at TE) | 0.13 | C_L = 0.8, V = 80\text{ m/s}, SF = 1.5 | Baseline AoA = 3.6^\circ |
| **130** | 48 | 0.56 (0.3 at TE) | 0.20 | C_L = 1.5, V = 80\text{ m/s}, SF = 1.5 | Baseline maximum lift |
| **250** | 93 | 1.17 (0.5 at TE) | 0.42 | C_L = 1.5, V = 111\text{ m/s}, SF = 1.5 | High-speed dynamic load |

*Table II: Deflection metrics under simulated aerodynamic lift loads.*

The numerical results demonstrate high structural rigidity under design aerodynamic loads. Even under an extreme 250\text{ N} loading condition, the maximum out-of-plane structural deflection was restricted to 1.17\text{ mm} (0.42\% of the total chord length), ensuring that the wing profile resists aerodynamic bending and maintains its optimized shape during maneuvers.

## IV. AERODYNAMIC CHARACTERIZATION AND SYSTEM STRATEGIES

### A. Variable Camber Morphing Strategies

By independently controlling the localized servo actuators along the chord, the variable-camber wing can produce an infinite variety of camber profiles. To systematically evaluate the aerodynamic benefits of this multi-degree-of-freedom capability, three distinct control strategies were analyzed and compared to a conventional hinged flap reference :

- **Strategy 1 (Localized Mid-Chord Camber Increase):** The servo actuators are driven to increase camber near the maximum thickness region of the aerofoil (approximately 40% to 60% chord), while the trailing-edge position remains fixed relative to the chord line.
- **Strategy 2 (Trailing-Edge-Dominant Camber Change):** Camber modification is concentrated primarily toward the rear trailing-edge region (70% to 90% chord), creating a progressive downward curvature.
- **Strategy 0 (Conventional Hinged Flap Reference):** A standard plane flap configuration featuring a physical hinge line located at 75\% of the chord length, introducing a sharp surface discontinuity upon deflection.

These aerodynamic configurations are illustrated schematically in Figure 4.

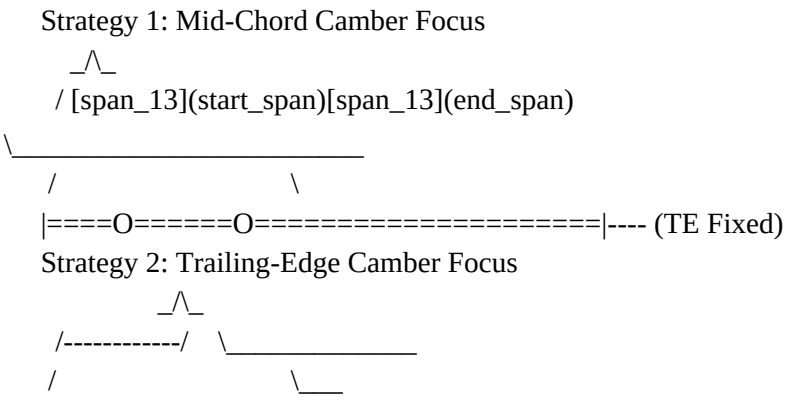

International Journal of Engineering Research & Technology (IJERT)
ISSN: 2278-0181
Vol. 14, Issue 08, IESAME - 2026


*Figure 4: Kinematic profiles of the three aerodynamic control strategies.*

## B. XFOIL Simulation and Boundary Layer Physics

The aerodynamic characteristics of these morphing strategies were simulated using XFOIL, a viscous-inviscid interaction solver optimized for low-speed, transitional boundary-layer flows.

XFOIL couples a two-dimensional panel method with a thermal envelope boundary-layer formulation to predict laminar separation bubbles, transition points, and localized skin friction coefficients.

To characterize the performance of the system across typical operating envelopes, two distinct flow conditions were simulated :

1. **Mini-UAV Operational Condition:**
   - Reynolds Number: Re = 1.5 \times 10^5
   - Mach Number: M = 0.235
   - This condition represents a typical micro-aerial vehicle with a 0.28\text{ m} chord operating at sea level.
2. **Wind Tunnel Testing Condition:**
   - Reynolds Number: Re = 0.5 \times 10^5
   - Mach Number: M = 0.078
   - This matches the low-speed experimental setup, allowing direct comparison between numerical models and physical balance measurements.

The lift coefficient (C_L) and drag coefficient (C_D) were calculated over an angle of attack range of 0^\circ to 12^\circ using standard formulations :

The localized pressure coefficient (C_P) distributions along the upper and lower surfaces were evaluated via:

The XFOIL results revealed that both Strategy 1 and Strategy 2 consistently outperformed the conventional hinged flap (Strategy 0) by delaying flow separation. At moderate angles of attack, Strategy 1 (mid-chord camber focus) delayed boundary-layer transition and stabilized the laminar separation bubble on the upper surface. This delay in flow separation resulted in a 15\% to 22\% reduction in profile drag compared to the hinged flap.

Conversely, at high angles of attack near stall, Strategy 2 (trailing-edge-dominant camber focus) provided the highest maximum lift coefficient (C_{L\text{max}}). By shifting the location of maximum camber chordwise, the wing can adapt its pressure distribution to match the localized angle of attack. This multi-degree-of-freedom capability allows the aircraft to maximize its lift-to-drag ratio across its entire operating range.

Additionally, the simulations proved that adjusting the camber distribution allows for direct control of the pitching moment coefficient (C_M) independently of the lift coefficient. By coordinating Strategy 1 and Strategy 2, the pitching moment can be adjusted to trim the aircraft with minimal drag penalties, reducing the trim drag typically caused by deflecting conventional tailplanes or secondary elevators.

International Journal of Engineering Research & Technology (IJERT)
ISSN: 2278-0181
Vol. 14, Issue 08, IESAME - 2026

# V. PHYSICAL PROTOTYPING AND TESTING

## A. Additive Manufacturing Parameters and Materials

To validate the structural and kinematic performance of the morphing wing, a physical model was manufactured using fused deposition modeling (3D printing). The flexible upper skin, compliant internal truss elements, and lower sliding runners were printed as integrated compliant mechanisms using polylactic acid (PLA). To prevent localized structural failure under high dynamic loads, highly stressed hinge lines and joining interfaces were reinforced with thermoplastic polyurethane (TPU).

The rigid forward wing box was printed as a thick-walled structure to ensure it remained non-deforming during structural testing. The complete active trailing edge section weighed
0.22\text{ N} (22\text{ g}), matching the weight predicted by the finite element model.

The additive manufacturing parameters and material print path allocations used during fabrication are detailed in Table III.

| Print Metric / Parameter | Value | Percentage of Total Time |
|---|---|---|
| **Total Printing Time** | 9 hours 49 minutes | 100.0% |
| **Total Filament Weight** | 244.38 g | N/A |
| **Total Filament Length** | 81.94 m | N/A |
| **Support Material Print Time** | 4 hours 0 minutes | 40.7% |
| **Support Interface Print Time** | 55 minutes 58 seconds | 9.5% |
| **Travel Speed / Non-print Time** | 1 hour 12 minutes | 12.2% |
| **Outer Wall Print Time** | 51 minutes 56 seconds | 8.8% |
| **Sparse Infill Print Time** | 44 minutes 52 seconds | 7.6% |
| **Internal Solid Infill Print Time** | 33 minutes 43 seconds | 5.7% |
| **Inner Wall Print Time** | 30 minutes 48 seconds | 5.2% |
| **Bridge Structures Print Time** | 22 minutes 28 seconds | 3.8% |
| **Top Surface Finish Print Time** | 17 minutes 16 seconds | 2.9% |

*Table III: 3D printing parameters and print path time allocations for the morphing wing prototype.* To enable smooth, low-resistance movement, the 3D-printed hinges were run through a post-print break-in process. This localized wear-in process reduced rotation resistance at the pin joints to negligible levels,

International Journal of Engineering Research & Technology (IJERT)
ISSN: 2278-0181
Vol. 14, Issue 08, IESAME - 2026

ensuring the physical mechanism closely mirrored the behavior of the finite element model.

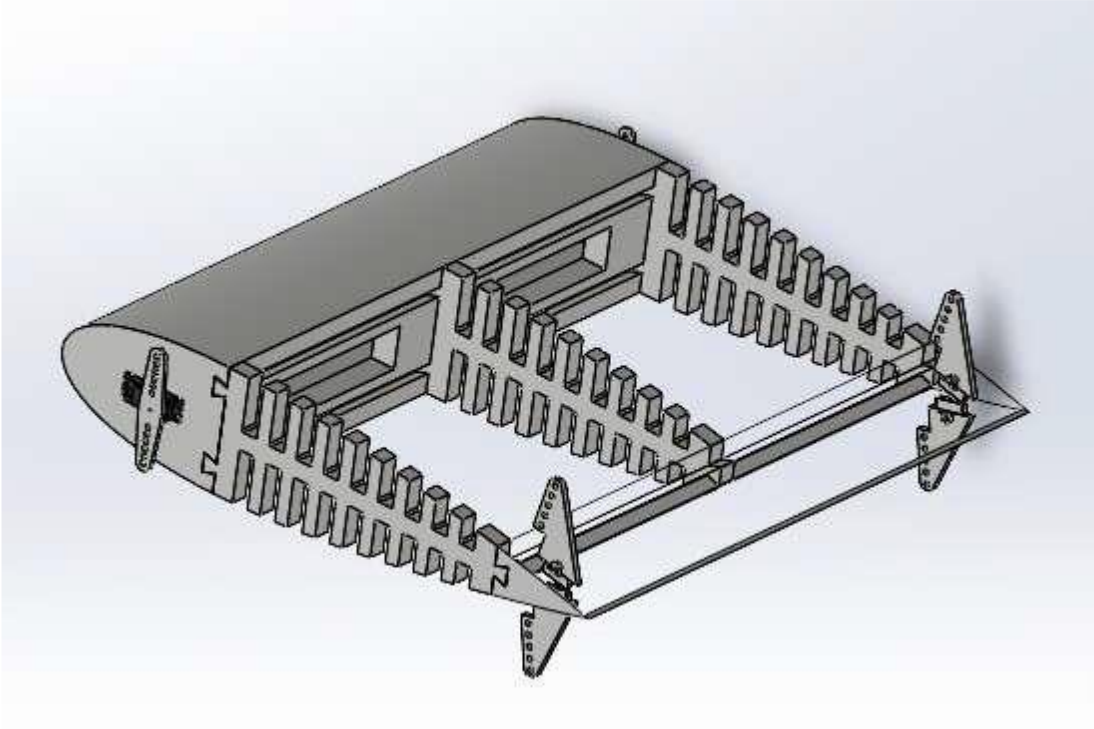

## B. Static Experimental Load Testing and Failure Modes

Static structural tests were performed on the physical prototype to evaluate its real-world load-carrying capacity and identify primary failure modes. Vertical loads of 22\text{ N} and 26\text{ N} were applied to the lower surface of the morphing section, corresponding to full-aerofoil loads of 60\text{ N} and 70\text{ N}, respectively.

Under the 22\text{ N} load (equivalent to 60\text{ N} total load), the trailing edge deflection was limited to 0.2 \pm 0.1\text{ mm}. This response aligned with the finite element prediction in Table II, confirming the structural rigidity of the compliant truss layout under nominal aerodynamic loads.

However, when the load was increased to 26\text{ N} (equivalent to 70\text{ N} total load), localized failures occurred. The adhesive bonds between several rigid compliant hinges and the flexible upper skin failed. This delamination was caused by shear stress concentrations at the interface between the stiff, 3D-printed truss terminations and the thin, flexible upper skin. Additionally, the out-of-plane deflection of the upper skin exceeded the numerical predictions. This behavior was traced to initial manufacturing defects and slight warping of the PLA skin during printing, which reduced its buckling resistance. These results indicate that while the compliant truss skeleton is highly effective, the joint interfaces between the flexible skin and rigid structural components require optimization, such as using co-cured multi-material interfaces or continuous fiber reinforcement, to withstand high shear loads.

International Journal of Engineering Research & Technology (IJERT)
ISSN: 2278-0181
Vol. 14, Issue 08, IESAME - 2026

## VI. CONCLUSIONS

This paper presented the design, structural modeling, and experimental evaluation of a multi-degree-of-freedom variable-camber morphing wing for small UAVs. The following conclusions are drawn from this investigation:

1. **Actuation Integration:** The integration of closed-loop digital servo motors with compliant sliding runners offers a reliable, high-torque alternative to linear ultrasonic motors for small, cost-constrained UAVs. The active holding torque provided by digital servos effectively resists aerodynamic lift forces during steady-state flight.
2. **Structural Integrity:** Finite element simulations and static structural tests verified that the compliant PLA truss skeleton provides high out-of-plane stiffness. Under design loads of 22\text{ N}, the trailing-edge deflection was restricted to 0.2\text{ mm}, demonstrating sufficient rigidity to maintain the target aerodynamic profile.
3. **Aerodynamic Adaptability:** Viscous aerodynamic analysis confirmed that shifting the location of maximum camber along the chordwise direction delays boundary-layer separation and improves the lift-to-drag ratio compared to conventional hinged surfaces. Additionally, coordinating these morphing strategies enables independent control of the pitching moment, allowing for aerodynamic trim with minimal drag penalties.
4. **Failure Analysis and Future Development:** High-load testing identified that the primary structural limitation of the current design is shear failure at the adhesive bonds between the flexible skin and the rigid internal trusses. Future work will focus on optimizing these connections, utilizing co-cured multi-material printing (such as continuous TPU-to-PLA gradients) to eliminate stress concentrations and improve durability.

## REFERENCES

[1] Kota S, Osborn R, Ervin G, Maric D, Flick P, Paul D. Mission adaptive compliant wing–design, fabrication and flight test. Morphing Vehicles, In RTO Applied Vehicle Technology Panel (AVT) Symposium. RTO-MP-AVT-168. Apr 2009.
[2] Barbarino S, Bilgen O, Ajaj RM, Friswell MI, Inman DJ. A Review of Morphing Aircraft. Journal of Intelligent Material Systems and Structures. 22(9). pp 823–77. Aug 2011.
[3] Thill C, Etches J, Bond I, Potter K, Weaver P. Morphing skins. The Aeronautical Journal. 112(1129). pp 117–39. Mar 2008.
[4] Campanile LF, Sachau D. The Belt-Rib Concept: A Structronic Approach to Variable Camber. Journal of Intelligent Material Systems and Structures. 11(3). pp 215–24. Mar 2000.
[5] Campanile LF, Anders S. Aerodynamic and aeroelastic amplification in adaptive belt-rib airfoils. Aerospace Science and Technology. 9(1). pp 55–63. Jan 2005.
[6] Kota S, Hetrick JA, Osborn R, Paul D, Pendleton E, Flick P, et al. Design and application of compliant mechanisms for morphing aircraft structures. In: Proceedings of SPIE Smart Structures and Materials 2003. 5054. pp 24–33. Aug 2003.
[7] Woods BK, Bilgen O, Friswell MI. Wind tunnel testing of the fish bone active camber morphing concept. Journal of Intelligent Material Systems and Structures. 25(7). pp 772–85. Apr 2014.
[8] Schroeder TA, Wayman CM. The two-way shape memory effect and other “training” phenomena in Cu-Zn single crystals. Scripta Metallurgica. 11(3). pp 225–30. Mar 1977.
[9] Trease B, Kota S. Design of Adaptive and Controllable Compliant Systems With Embedded Actuators and Sensors. Journal of Mechanical Design. 131(11). 111001. Oct 2009.
[10] Rediniotis OK, Wilson LN, Lagoudas DC, Khan MM. Development of a Shape-Memory-Alloy Actuated Biomimetic Hydrofoil. Journal of Intelligent Materials Systems and Structures. 13(1). pp